FULL PAPER

Cite this: DOI: 00.0000/xxxxxxxxxx

Design and Fabrication of a Novel On-Chip Pressure Sensor for Microchannels.†

Nishagar Raventhiran, Razin Sazzad Molla, Kshithij Nandishwara, Erick Johnson and Yaofa Li*

Received Date
Accepted Date

DOI: 00.0000/xxxxxxxxxx

Pressure is important in virtually all problems in fluid dynamics from macro-scale to micro/nano-scale flows. Although technologies are well developed for its measurement at the macroscopic scale, pressure quantification at the microscopic scale is still not trivial. This study reports the design and fabrication of an on-chip sensor that enables quantification of pressure in microfluidic devices based on a novel technique called astigmatic particle tracking. With this technique, thin membranes that sense pressure variations in the fluid flow can be characterized conveniently by imaging the shapes of the particles embedded in the membranes. This innovative design only relies on the reflected light from the back of the microchannel, rendering the sensor to be separate and noninvasive to the flow of interest. This sensor was then applied to characterize the pressure drop in single-phase flows with an accuracy of ∼70 Pa and good agreement was obtained between the sensor, a commercial pressure transducer and numerical simulation results. Additionally, the sensor successfully measured the capillary pressure across an air-water interface with a 7% deviation from the theoretical value. To the best of our knowledge, this pore-scale capillary pressure quantification is achieved for the first time using an on-chip pressure sensor of this kind. This study provides a novel method for in-situ quantification of local pressure and thus opens the door to a renewed understanding of pore-scale physics of local pressure in multi-phase flow in porous media.

1 Introduction

Pressure measurement is of crucial importance in fluid mechanics to describe and understand various flows. In particular, precise measurement and control of pressure with high spatial and temporal resolutions in microfluidic systems are key to numerous scientific and engineering applications, ranging from sample manipulation in biological studies [1–4] to the evaluation of capillary pressure in multi-phase flow in porous media, which is relevant to applications like tissue engineering, biological flows, CO_2 sequestration and even enhanced oil recovery (EOR). [5–7] For instance, capillary pressure is central to the description of multi-phase flow in porous media [8–15]. Conventional mathematical models of multi-phase flow in porous media have been inevitably relying on empirical relations of capillary pressure which are well known to be hysteretic [8,9]. It is increasingly accepted that direct *in-situ* measurement of capillary pressure at the microscopic scale will be extremely valuable to mitigate such hysteresis and thus achieve a unique description of the state of the porous medium flow system. [16–18] As another example, in evaporative cooling [19–21] and flow boiling heat transfer [22], local vapor pressure in a bubble plays an important role in bubble growth and departure dynamics, which defines the overall heat transfer performance, thus rendering pressure characterization at the microscopic level a critical need to achieve a fundamental understanding of flow evaporating and boiling processes.

Currently, a number of miniature pressure sensors are commercially available with the advancement of technologies including piezoresistive, capacitive, optical, interferometric and optofluidic pressure sensors. [23,24] However, direct integration of such sensors into microfluidic devices can be challenging because of their still relatively large sizes compared with typical microchannels. Additionally, multi-step fabrication processes are often required to enable such integration. [18] Therefore, direct on-chip pressure sensors become highly promising and desirable.

In the past two decades, several on-chip pressure measurement methods have been developed employing various working principles. Abkarian et al. [25] were among the first ones to contribute to this advances, and they designed a differential manometer based on the interface movements between two immiscible fluids in a microchannel. Alternatively, Shen et al. [26], Srivastava and Burns [27], and Hoera et al. [28] took advantage of the compressibility of air to measure pressure in the target channel by monitoring the volumetric response of an air bubble that was intentionally

Mechanical & Industrial Engineering Department, Montana State University, Bozeman, Montana, USA. Fax: 406-994-6292; Tel: 406-994-6773; E-mail: yaofa.li@montana.edu

* Corresponding author.

† Electronic Supplementary Information (ESI) available: [details of any supplementary information available should be included here]. See DOI: 00.0000/00000000.

trapped in a side cavity. Probably the most popular design is the membrane-based approach. The basic idea of this design is to create a thin membrane adjacent to the target microchannel as the sensing element that deflects subject to pressure variation in the target microchannel. The membrane deflection can be read out optically or electrically, which is then correlated to the actual pressure change through a calibration step. Silicon[29] and polydimethylsiloxane (PDMS)[17,23,30,31] are among the most common materials for building such membranes for their low cost and ease of fabrication.

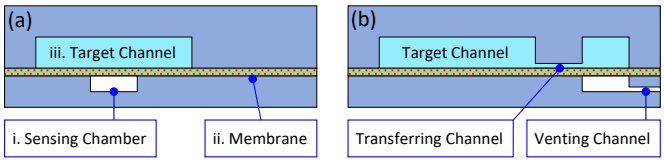

Fig. 1 Schematic diagrams illustrating the basic elements in a typical membrane-based pressure sensor: (a) a design with a closed sensing chamber directly below the target channel, and (b) a design with an open sensing chamber placed remotely to the side of the target channel.

A typical membrane-based pressure sensor consists of three layers as illustrated in Figure 1a: (*i*) a bottom layer embedded with pressure taps called sensing chambers of hundreds of micrometers thick; (*ii*) a sensing PDMS membrane with a thickness ranging from a few to several tens of micrometers; (*iii*) and a top layer containing the target channel whose thickness can range from a few micrometers to a few millimeters depending on its intended function. The three layers are often fabricated separately and then assembled employing plasma assisted bonding. While certain designs put the sensing chambers directly above or below the target flow channel[30] (*c.f.* Figure 1a), others connect the sensing chambers and the target channel *via* auxiliary transferring channels to make room for signal readout as illustrated in Figure 1b.[31] The sensing chambers can be either closed or open to the atmosphere through a venting channel, with the latter resulting in a constant pressure within the sensing chambers, which has been shown to increase the measurement sensitivity (*c.f.* Figure 1b).[30]

With the three-layer design, pressure measurement is conveniently transformed into quantification of membrane deflection, which has been achieved *via* approaches mainly falling into two categories: the optical schemes and the electrical schemes. The optical schemes often use a microscope and a camera to correlate the membrane deflection with a certain optical output, such as image intensity[32], contrast[23] or interference patterns[30]. Orth et al.[17] characterized membrane deflection based on the goodness of focus of a reference target. When coupled with transmitted light, the membrane effectively works as a lens, which changes the optical path as deflection is increased under increasing pressure, causing the focal plane and image focus to shift accordingly. The similar idea was adopted by Chaudhury et al. in a later study[23], where membrane deflection was instead inferred based on image contrast. Song and Psaltis[30] leveraged interferometry, where the membrane, upon illumination by monochromatic light, generates interference patterns that depend on pressure. Chung et al.[31] leveraged a suspension of fluorescent particles and creatively measured membrane deflection through the amount of depleted fluorescent particles in the sensing chamber. In general, optical schemes are accurate and easy to set up, as the required equipment (*e.g.*, cameras and microscopes) is in many cases already available in those experiments (*e.g.*, for flow or cell visualization). On the other hand, the electrical schemes detect the change of electrical resistance[33–36] or capacitance[37,38] to infer the membrane deflection. While the electrical schemes need no more than a simple circuit and a multimeter to perform the measurement, the fabrication of the devices can be much more complicated due to the requirements of on-chip electrodes and other electrical elements. It is worth noting that recently the use of liquid metals has made such fabrication significantly easier for individual pressure sensors as illustrated by Zhou et al.[39] and other researchers[33,36]. However, when multiplexed microscale sensors (*i.e.*, an array or matrix of *independent* sensors) are needed, the electrode matrix, lead wires and sensing channels can still be challenging to fabricate on polymer membranes such as PDMS.

Although these previous designs have greatly improved our ability to characterize pressure in various microfluidic devices, we note that none of them seems to be suited to our specific application. That is to map capillary pressure distribution in multiphase flow in porous media[11,15]. For instance, many previous designs used auxiliary/transferring channels to facilitate signal readout, which however adds significant dead volume to the system and thus reduces the responsiveness of the sensors.[31] Additionally, many designs used transmitted light for signal readout[17,23], where illumination light runs through all three layers: the membrane, the sensing chamber and the target channel. In that case, the output signal can be significantly affected by the flow pattern within the target channel, rendering them not suitable for measurement of multi-phase flows. Moreover, while several studies demonstrated multiplex pressure measurement, a majority of previous designs only perform single-point measurements as opposed to pressure field mapping. To overcome these challenges, this work proposes a novel design of microfluidic pressure sensor to achieve fast and precise pressure measurement in microchannels. In this current design, the membrane deflection will be detected through particle astigmatism inspired by the astigmatic particle tracking velocimetry (APTV)[40,41], which offers the benefits of simpler fabrication, easier implementation and better versatility. The innovation of current work is two-fold: (*i*) we have successfully demonstrated the effectiveness of APTV in the quantification of membrane deflection and pressure measurement; (*ii*) we have, to the best of our knowledge, for the first time applied such pressure sensors to capillary pressure quantification in mulitphase flow. This work thus paves the way for 2D pressure field mapping in porous medium flows.

2 Experimental Description

2.1 Pressure Sensor Design

Our membrane-based pressure sensor also consists of three layers, as shown in Figure 2a. Compared with previous designs, the novel aspect of this design is that 1 μm fluorescent particles are embedded into the sensing membrane to facilitate characteriza-

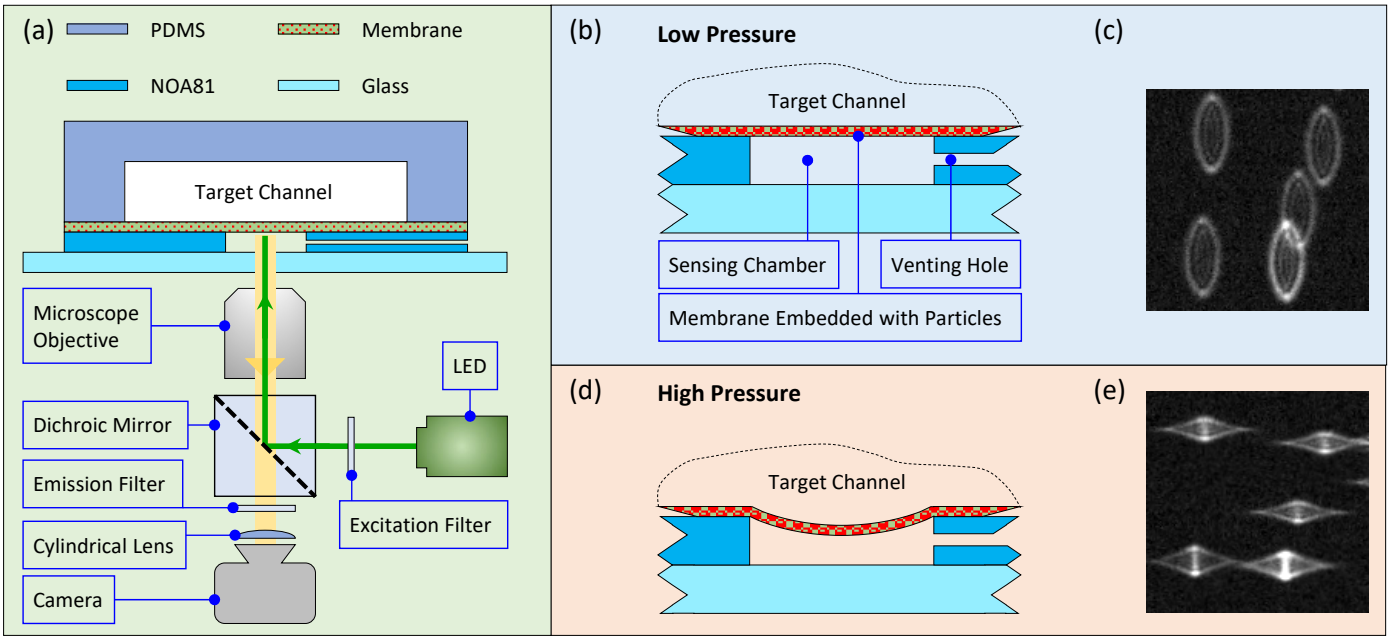

Fig. 2 (a) A schematic diagram illustrating the three-layer design of our pressure sensor: the top layer contains the flow channel made of PDMS; the middle layer is PDMS membrane with fluorescent particles embedded within; and the bottom layer contains the sensing chamber fabricated in optical glue (NOA81). Note that a glass slide is used to serve as a rigid substrate to minimize deformation of the device. (b, c) the state of the membrane and the corresponding particle images when the device is subject to *low* pressures. (d, e) the state of the membrane and the corresponding particle images when the device is subject to *high* pressures.

tion of membrane deflection using the astigmatic particle tracking technique (see details below in § 2.2). Briefly, when the applied pressure is low, the membrane sits close to its initial position, which is far from the microscope objective (note the objective views from the bottom), causing the embedded particles to form vertical elliptical images on the camera (Figure 2b, c). As the applied pressure increases, the membrane deflects and carries the embedded particles towards the microscope objective to form horizontal elliptical images (Figure 2d, e). Essentially, the membrane deflection and thus the applied pressure are measured through the shapes of particle images. The sensing chambers placed right below the target channel are all connected to the atmosphere allowing them to stay at atmospheric pressure throughout the experiment.[17] This design offers several benefits. It allows for pressure measurement at virtually any location of the target channel by conveniently positioning the sensing chamber below the desired location, and even 2D pressure fields can be obtained by incorporating a matrix of sensing chamber without any modification of the setup for signal readout. By leveraging APTV, image acquisition can be performed using any standard epi-fluorescence microscope with minimal modification. Additionally, the sensor sensitivity and measurement range can be finely tuned by varying the sensing chamber size or membrane thickness. It is also worth noting that, although this study focuses on the measurement of positive pressures in the target channel, this design is indeed capable of measuring negative gauge pressures without needing any modification. Under negative pressures, the membrane would deflect upward, causing the elliptical particle images (*c.f.* Figure 2c) to be even slenderer, from which and the calibration images, the corresponding negative pressure can be quantified.

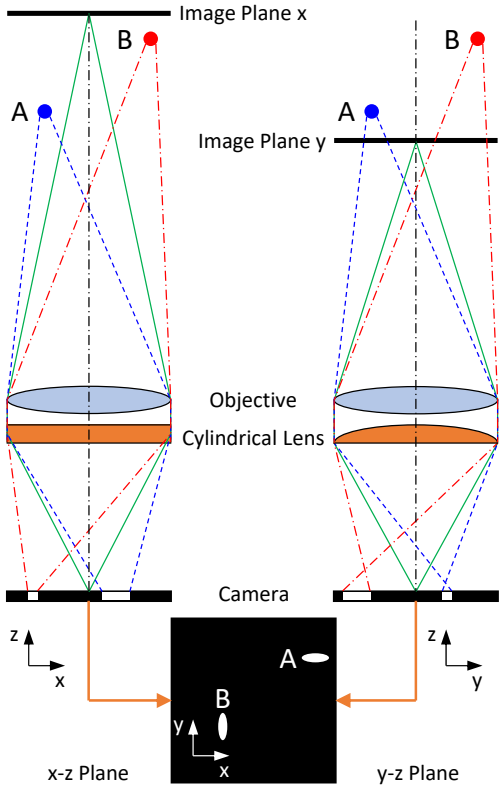

Fig. 3 A schematic illustrating the working principle of astigmatism.[40]

2.2 Astigmatic Particle Tracking

As mentioned previously, one of the innovative aspects of the design is the use of the APTV technique for membrane deflection quantification.[40] To achieve that, (*i*) fluorescent tracer particles are embedded in the membrane during fabrication, and (*ii*) a cylindrical lens was placed between the microscope objective and the camera as a modification to standard microscopy. As shown in Figure 3, the cylindrical lens, which focuses light within a single axis only, causes the imaging plane to shift in the x-z plane, without affecting the y-z plane. Particles at different z locations, will be focused differently in both x and y directions, forming different shapes of images depending on their z locations. Assuming that there is no relative movement between the particles and the membrane, particle position effectively yields information about membrane deflection. In this current configuration, a particle that is far away from the objective (*i.e.*, higher z location), form vertically elongated images (particle B in Figure 3), whereas a particle that is close to the objective tends to form horizontally elongated images (particle A in Figure 3).

2.3 Fabrication

The device was fabricated in separate layers, which were then assembled by bonding all layers together as shown in Figure 4. The microchannel (Layer I) was fabricated employing standard soft lithography[42], which consists of three major steps: photomask design, SU-8 master fabrication and PDMS molding (Figure 4, Layer I). The photomask was designed in Adobe Illustrator®, and printed by a third-party company (CAD/Art Services, Inc.). To create the master, a layer of SU-8 3050 (Kayaku Advanced Materials SU-8 3050) was coated on a 4" silicon wafer by spinning it at 1000 rpm for 30s, following which a series of processes including soft baking, exposing, post exposure baking, developing, cleaning, and hard baking were performed sequentially, to achieve the designed pattern with a final nominal film thickness of 100 μm. The SU-8 master was then silanized using Trichlorosilane (Sigma-Aldrich 1H,1H,2H,2H-perfluorooctyl) for 30 min. Meanwhile, the PDMS polymers were prepared at a ratio of 10:1 (pre-polymer:scuring agent), mixed, and degassed for 30 min to remove all air bubbles entrained in the polymer during mixing. Finally, the polymer was poured on top the SU-8 master, and baked at 65 °C for 2 hours to cure, following which the PDMS slab was peeled off the SU-8 master, cut into individual devices, and 2 mm holes were punched to serve as fluid delivery ports.

The membrane fabrication was conducted employing the spin-coating technique as shown in Figure 4 (Layer II). The goal here is to create a flexible PDMS membrane of approximately 5 μm in thickness with 1 μm fluorescent particle embedded within. To this end, the PDMS mixture prepared again at the 10:1 ratio was diluted by tert-butyl alcohol (TBA, $(CH_3)_3COH$) at a ratio of 1:3 by weight (*i.e.*, 1 part of PDMS and 3 parts of TBA). TBA is a tertiary alcohol and can be used to reduce the viscosity of the PDMS mixture without causing swelling to the final cured product, which is critical to create thin PDMS films as needed here.[43] Then 20 μl suspension of carboxylate-modified fluorescent particles of 1 μm in diameter (FluroSpheres, F8819) was added into 8 ml diluted PDMS polymer and mixed with the aid of ultrasound. The final mixture was then poured onto a silanized bare silicon wafer and spun at 2000 rpm for 5 min. The PDMS film was then baked for 8 minutes at 65 °C to semi-cure. The microchannel (Layer I) fabricated in the previous step was then bonded to the membrane by slowly and steadily placing it onto the membrane. In this regard, the semi-cure process of the membrane is critical as it ensures the PDMS membrane to solidify but still sticky enough to create good bonding between the two layers. The assembly of the membrane and microchannels was fully cured in the oven for another 2 hours at 65 °C.

For the sensing chambers (Layer III), a PDMS mold containing the sensing chamber design was first fabricated with the same procedures used in Layer I, following which optical glue molding was conducted. The PDMS mold was placed on a flat surface with the patterned side facing up. Two drops of optical glue (Norland Optical Adhesive 81) were dispensed onto the PDMS surface. Then a clean microscope slide (Fisher Scientific 75×25 mm 144/GR) was placed on top of the optical glue and gently pressed down to ensure the glue evenly spreads between the PDMS mold and the microscope slide. The whole assembly was then exposed under UV light (Thorlabs M385LP1) for 10 minutes. Once the glue was cured, the PDMS mold was peeled off to expose the sensing chambers made of optical glue. It is worth noting that, the sensing chambers could have been fabricated in PDMS too as in many previous studies[17,23,31]. In fact, PDMS sensing chambers were initially used in our device, and acceptable results were achieved. However, we note that the optical glue used herein offers much better optical properties compared with PDMS, which helped to significantly improve the final particle image quality and signal-to-noise ratio (SNR). In addition, sensing chambers made of optical glue can be easily peeled off the PDMS part, allowing for them to be reused in multiple devices. Finally, the top two layers (Layers I and II) were aligned and bonded with the third layer on an aligning stage (three way translation + rotation), and the nanoports were attached to the inlet and outlet of the microchannel to facilitate fluid delivery, which completes the device fabrication.

2.4 Device Calibration

In order to use the device for accurate pressure measurement, a relationship between the target pressure and membrane deflection needs to be pre-defined through a calibration step.[17,31] Herein the calibration procedure simply involves acquiring two sets of images of the membrane: (*i*) one set of images at a series of prescribed z positions, hereinafter referred to as the position calibration; and (*ii*) a second set of images of the membrane at a series of prescribed pressures, hereinafter referred to as the pressure calibration. The position calibration essentially creates a library of images containing information of particle image shapes at various distances from the microscope objective (Figure 5 [Left Column]). These images were used later as reference images (effectively a ruler) to determine the distance between the membrane and the microscope objective for real experimental images. In the position calibration, the objective was initially positioned

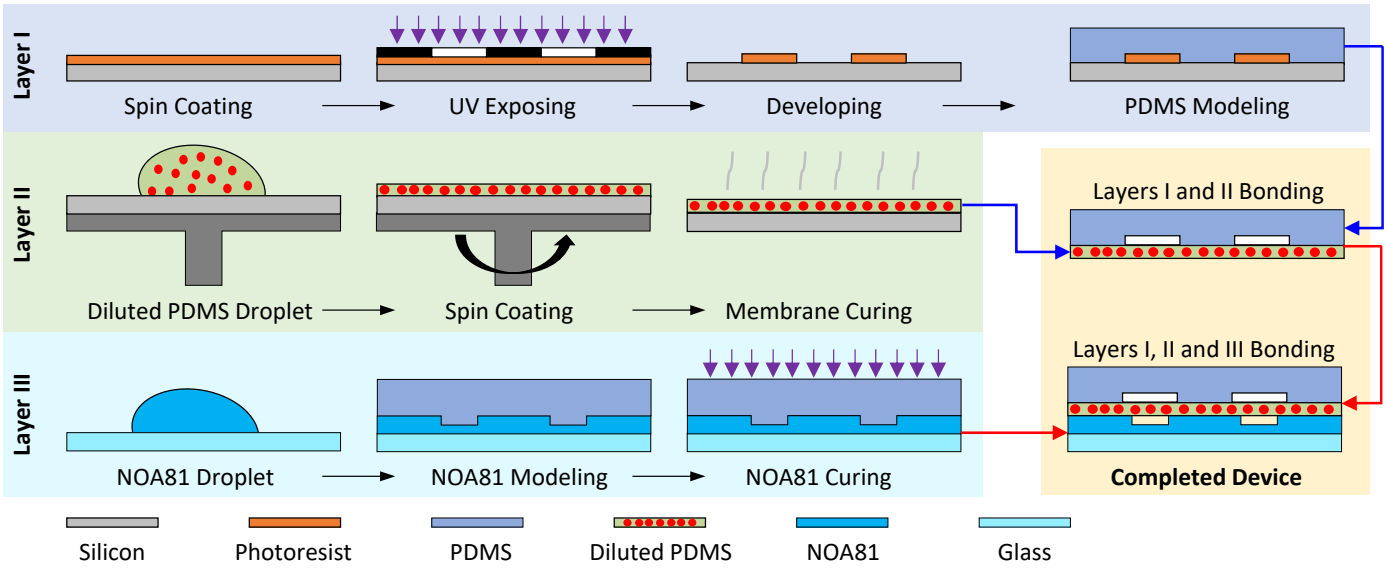

Fig. 4 Schematic illustrating the major steps to fabricate the device in layers.

at $z = 0\,\mu$m, and gradually moved up towards the device at an increment of $1\,\mu$m, which was precisely controlled by the focusing knob on the microscope. On the other hand, the pressure calibration creates a library of images at various prescribed pressures as shown in Figure 5 [Right Column]. To perform the pressure calibration, again the objective was initially positioned at $z = 0\,\mu$m with zero pressure applied to the device. Then the applied pressure was gradually increased at an increment of 100 Pa, which causes the membrane to deflect downward and get closer to the objective (note again the microscope is an inverted one). The applied pressure was controlled by varying the height of an elevated water tank which sustains hydrostatic pressure as shown in the † ESI (Figure S1). While the calibration process appears complicated, it really took no more than 15 min based on our repeated tests. As detailed below in image analysis, by properly correlating the two sets of particle images, a relation between the applied pressure and membrane deflection can be achieved, which will be crucial to inferring pressure measurement based on particle images in real experiments.

2.5 Image Acquisition and Analysis

To facilitate device calibration and actual measurement, particle images were acquired employing the epi-fluorescence technique relying on an inverted microscope (Olympus IX-71), a scientific CMOS camera (Phantom VEO 440), and a green LED (Thorlabs SOLIS-525C M00569931). The camera sensor consist of a matrix of 2560×1600 pixels of $10\times10\,\mu$m^2 each, resulting in a physical size of 25.6×16 mm^2, which, coupled with a 20x objective and 1.2x camera adaptor, produces a final field of view (FOV) of 1.06×0.67 mm^2. Unless otherwise noted, for each case a sequence of 100 images were acquired at a frame rate of 25 fps.

The images were processed using an in-house code in MATLAB R2019a. Briefly, a region of interest (ROI) of nominally 120×120 pixels was selected surrounding the center of the circular membrane. Extra care was used to make sure at least one fluorescent particle falls within the ROI. While a fluorescent particle does not need to be centered, the entire particle should be in view, and the size of the ROI should be adjusted accordingly. To

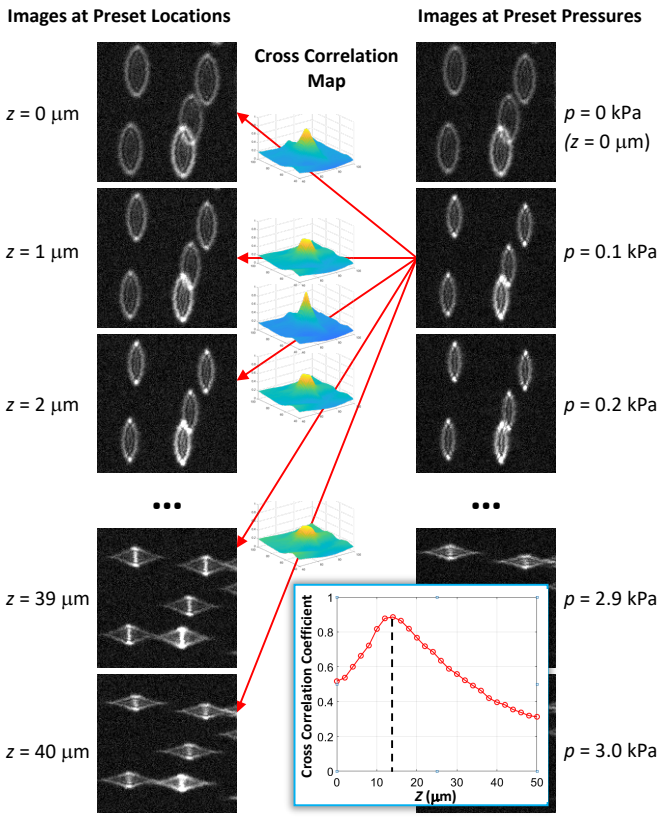

Fig. 5 A chart illustrating the calibration procedures. The left column contains the position calibration images, whereas the right column contains the pressure calibration images. Each image on the right is to be cross-correlated with all images on the left to identify the best match. The inset shows a sample fitted curve of the cross-correlation coefficients, and the uncertainty corresponding to Z position control is $0.5\,\mu$m.

process the calibrate images, the image acquired at each pressure (*e.g.*, $p = 0.1$ kPa in Figure 5) was cross-correlated with all position calibration images, and cross-correlation coefficients were calculated between the specific *pressure* calibration image and all *position* calibration images. Here the goal is to identify the position calibration image that is the most similar to the specific pressure calibration image, which is evaluated based on the cross-correlation coefficient (*i.e.*, a higher cross-correlation coefficient indicates a better similarity between two images). with all coefficients calculated, a polynomial curve was fitted using the built-in "polyfit" function in MATLAB to identify the best match based on the peak value of the curve (*c.f.* Figure 5 inset). Since the objective position is fixed in the pressure calibration, the z location of the identified position calibration image effectively measures the amount of deflection corresponding to the specific pressure calibration image. Using this approach, each pressure calibration image was matched with a position calibration image, essentially producing a relationship between the applied pressure and the membrane deflection (Figure 6).

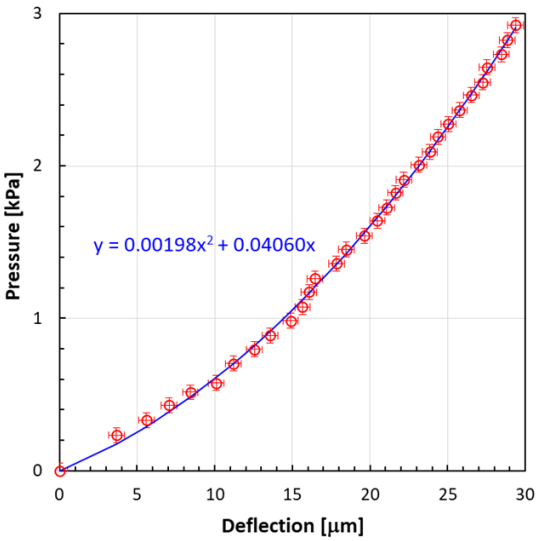

Fig. 6 Calibrated relationship between applied pressure (kPa) and membrane deflection (μm) obtained for one pressure sensor used in this study. The horizontal error bars represent the uncertainty of Z position control (*i.e.*, 0.5 μm) and the vertical error bars represent the uncertainty of hydrostatic pressure control (*i.e.*, 0.05 kPa).

Processing of an actual measurement image taken at an unknown pressure essentially follows the same way. The target image at the unknown pressure (*i.e.*, to be measured) again was cross-correlated with all position calibration images, and cross-correlation coefficients were calculated. The position calibration image that yields the highest coefficient was then identified, which effectively measures the amount of deflection corresponding to the target image. The deflection was then substituted into the pressure-deflection relation obtained in the calibration step (*i.e.*, Figure 6) to determine the unknown pressure, which completes the measurement.

3 Results and Discussion

3.1 Calibrated Pressure-Deflection Relation

Figure 6 shows the pressure–deflection relation obtained for one pressure sensor, which was calibrated in the range of 0–2.9 kPa. As expected, the applied pressure and membrane deflection show good linearity for small deflection in the pressure range of 0–1 kPa with a sensitivity of ~0.066 kPa/μm. In the higher pressure range, non-linearity starts to arise with an average sensitivity of 0.13 kPa/μm. To facilitate pressure calculation and interpolation, a second order polynomial was used to fit the data in the entire range of 0–2.9 kPa. The root mean square deviation (RMSD) between the data points and the fitted curve is less than 0.04 kPa, corresponding to ~1.4% of the full-scale value of 2.9 kPa. It is worth noting that in the current study, all the membranes and sensing chambers were fabricated following exactly the same procedures and recipes in a highly repeatable manner, so the calibration curves are highly similar between different devices and different sensors. While it is possible to use the same calibration curve for all sensors with acceptable accuracy, we produced a separate ad hoc calibration curve for each individual sensing chamber and membrane to ensure high accuracy. In addition, to rigorously test the pressure sensor for its robustness and potential hysteresis, a test calibration was also performed for 4 consecutive runs using a separate sensor fabricated in the same way, where the applied pressure was varied following a pattern of 0 kPa – 2.4 kPa – 0 kPa – 2.4 kPa – 0 kPa at a step of 0.2 kPa. As shown in † ESI Figure S5, the data from all 4 runs agrees very well, with a maximum RMSD of 0.042 kPa (1.75% of the calibrated range) between any two runs, suggesting a good repeatability and negligible hysteresis of the pressure sensor in the calibrated range.

3.2 Application: Pressure Drop in Single-Phase flow

As the first application and validation of the pressure sensor, the pressure drop in a microchannel was measured using both air and deionized (DI) water as the working fluids at constant flow rates. For this measurement, a microchannel of a nominal width, height and length of $w = 0.1$ mm, $h = 0.12$ mm, and $l = 18.8$ mm, respectively, were fabricated as shown in Figure 7. To the upstream and downstream of the test channel, two short channels with enlarged width ($w = 0.3$ mm) were added to connect the test channel with the inlet and outlet. The pressure sensors were then incorporated right at the upstream of the inlet and the downstream of the outlet to effectively measure the pressure drop across the entire test microchannel. It is worth noting that the test microchannel was intentionally designed to have a U shape to: (*i*) reduce the footprint of the device, and (*ii*) place the upstream and downstream sensors close by so that they can be measured simultaneously by fitting both in one FOV of the microscope. For all sensors used in this study, the sensing chambers were 200 μm in diameter, and ~80 μm in depth. As illustrated in Figure 7a, the flow was controlled by a high-precision syringe pump (Harvard Apparatus, PHD 22/2000). Additionally, the pressure different between the inlet and outlet was also measured by a commercial pressure transducer (Validyne, P55E) as a benchmark reference, whose reading was continuously logged using a data acquisition

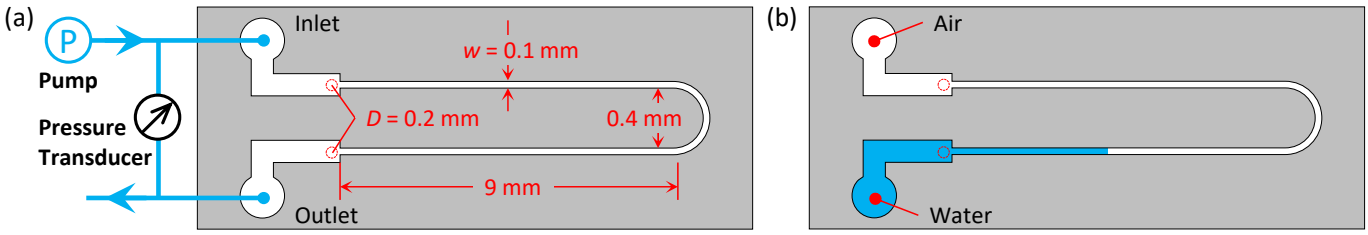

Fig. 7 Schematic illustrating the pressure drop measurement setup for the single-phase flow (a) and multi-phase flow (b) cases. The test microchannel is 0.1 mm wide, 0.12 mm depth and 18.8 mm long. And the pressure sensors used herein are all 0.2 mm in diameter. The flow rate is controlled by a syringe pump connected to the inlet of the microchannel, whereas the outlet is opened to atmosphere. In the single-phase flow case, the pressure drop across the microchannel is also measured with a differential pressure transducer. In the multi-phase flow case, air was used to displace water at a very low flow rate, and the pressure drop is dominated by the capillary pressure jump across the interface.

system (National Instruments, USB-6001).

For the air flow experiment, the pressure drop was measured at flow rates from 0 to 1.2 ml/min with an increment of 0.1 ml/min. The Reynolds number at the maximum flow rate of 1.2 ml/min was calculated to be 11.6 based on the hydraulic diameter of the microchannel, confirming the laminar flow conditions. Following each increase of flow rate, a minimum waiting time of 1 min was used to ensure a steady-state flow during image acquisition. The same MATLAB image analysis algorithm as described in the calibration procedures was used to calculate the membrane deflection for each applied flow rate. Once the membrane deflection was determined, it was substituted into the pressure-deflection relation (*i.e.*, Figure 6) to determine the pressure exerted at each of the pressure sensors at upstream and downstream. The difference between the two pressures yielded the pressure drop across the microchannel.

Figure 8a shows the variation of pressure drop within the microchannel as a function of flow rate. As expected for laminar flows, the pressure drop is proportional to the flow rate, resulting in a linear relationship. The error bars represent the combined error propagated from uncertainties in the calibration relation and uncertainties in the membrane deflection calculation. To validate the pressure sensor measurement, it is compared with the data obtained with the commercial pressure transducer. It can be seen that the two sets of measurement agree very well yielding a RMSD of 0.028 kPa and a maximum deviation of 0.045 kPa, ∼1.5% of the full scale value. To further validate the experimental measurement, the pressure drop across the microchannel was also numerically calculated using Star-CCM+ (see † ESI for details), which was plotted in Figure 8. The numerical results agrees reasonably well with the experimental measurements with a slight overprediction at the high pressure range. Although this overprediction is within the measurement uncertainty, we believe this discrepancy can also be partially attributed to the slight deformation (expansion) of the PDMS microchannel under high pressures[44], which was not considered in the simulation. We also note that the pressure drop in a rectangular channel at a given flow rate can also be theoretically calculated based on the following equation[45],

$$\Delta p = \frac{4\mu l}{wh^3[\frac{1}{3} - \frac{64h}{\pi^5 w} tanh(\frac{\pi w}{2h})]} Q \quad (1)$$

where μ is the dynamic viscosity of the working fluid, and Q is the volumetric flow rate through the microchannel. Although data is not shown here, the theoretical values are also in reasonable agreement with the experimentally measured values. However, after careful measurement, it was observed that the microchannel used herein does not have a perfect rectangular cross-section. Instead the cross-sectional is more of a trapezoid shape with curved edges (see † ESI Figure S2). Therefore, we believe the numerical simulation result, which was based on the actual 3D geometry of the microchannel, provides a better representation of the actual pressure drop in the microchannel as shown in Figure 8a.

The same experiment was performed using DI water as the working fluid at different flow rates. Due to the much higher dynamic viscosity of water compared with air, the flow rate was reduced by about two orders of magnitude, so that the pressure drop falls within the measurement range of the sensors. The Reynolds number corresponding to the highest flowrate is 1.4, again confirming laminar flows in the microchannel. Figure 8b shows the variation of pressure drop within the microchannel as a function of flow rate using DI water as the working fluid. Again a good linear relationship between pressure drop and flow rate is evident, as expected for laminar flows. All three sets of data show reasonably good agreement, with a RMSD value of 0.036 kPa between the pressure sensor and pressure transducer measurements. It is also worth noting that, to quantify the potential hysteresis of the pressure sensor, pressure drop was also measured by reducing the flow rate from high to low at selected flow rates (*i.e.*, 1.2 ml/min back to 0 ml/min at a step of 0.2 ml/min in the air case, and 8 μl/min back to 0 μl/min at a step of 2 μl/min in the water case). The maximum deviations between the up and down runs are 0.04 kPa and 0.03 kPa for the air and water cases, respectively, which both fall within the measurement uncertainty, confirming very little, if any, hysteresis of the pressure sensor.

3.3 Application: Capillary Pressure in Multi-Phase Flow

The capillary pressure measurement in an air-water multi-phase flow was conducted using a similar setup as used for the single-phase flow. To initiate the experiments, the microchannel was first presaturated with DI water using the syringe pump at a flow rate of 5 μl/min. Extra care was taken during this step to prevent any air bubbles from getting into the microchannel. Then the syringe pump was paused for a minimum of 5 min to allow the flow

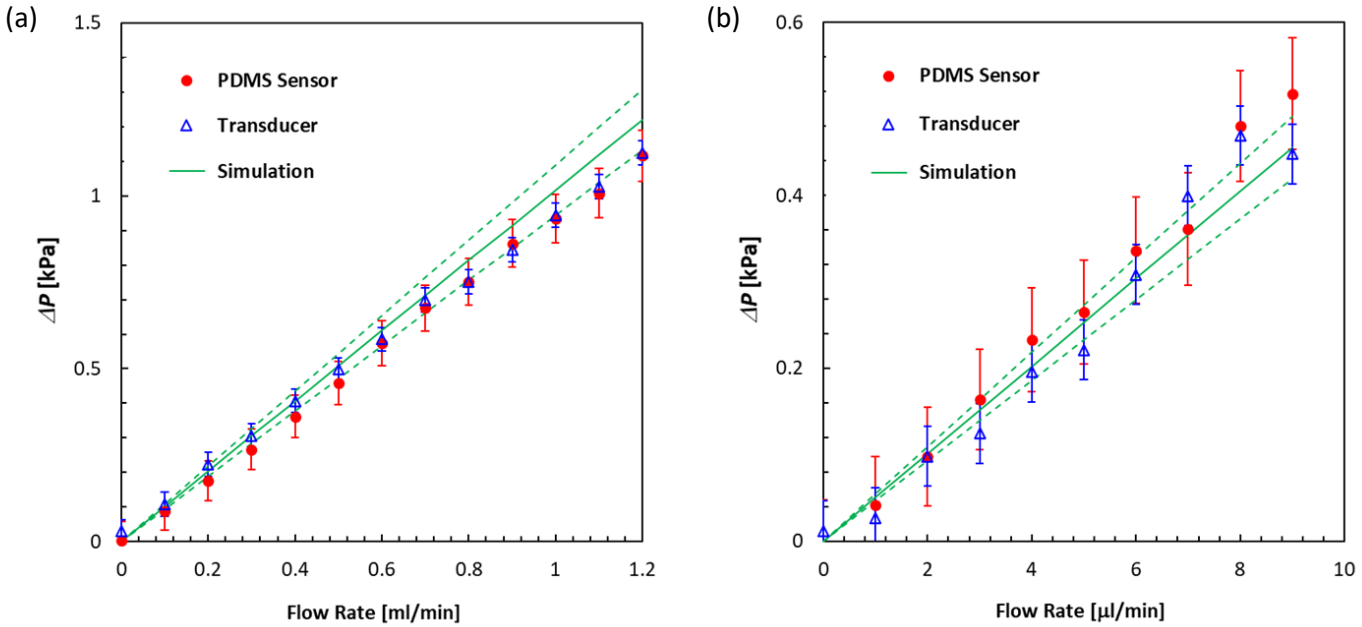

Fig. 8 Pressure drop at various flow rates obtained using our sensor (red symbols), the commercial pressure transducer (blue symbols) and numerical simulation (green lines) for the single-phase flows of air (a) and water (b). The error bars associated with the PDMS sensor data indicated the overall propagated uncertainties (0.07 kPa, ~2.4% of the full scale value) from the calibrate relation and membrane deflection measurement. The trsansducer data error bars are based on the manufacturer-specified accuracy. And the dashed lines are the upper and lower bounds of the numerical values (±8%), again based on propagated errors mainly from channel dimension measurements.

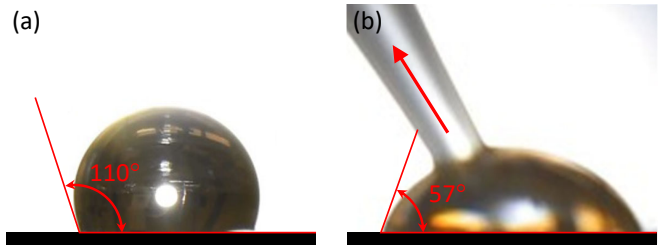

Fig. 9 Photos of water droplets on a PDMS surface under (a) static condition and (b) receding condition. To create the receding contact line, the water was instantaneously withdrawn from the droplet using a pipette. Both images were processed in ImageJ, and the static and receding contact angles turned out to be 110° and 57°, respectively.

to subside. Next air was slowly injected into the microchannel at the same flow rate of 5 μl/min. As the air enters the microchannel, an air-water interface is created, which generates a pressure jump (capillary pressure) across the interface due to surface tension and interfacial curvature. It is worth noting that PDMS is slightly hydrophobic under static conditions. In fact, our measurement shows that the static contact angle of water on PDMS surface is 110° (Figure 9a). However, in this case when water is being displaced out of the microchannel, what is relevant is the receding contact angle. Our measurement indicated a receding contact angle of 57° for a droplet water shrinking on PDMS surface (Figure 9b). The entire process of air displacing water was recorded and again processed in MATLAB as discussed earlier.

Figure 10 shows the raw particle images for both upstream and downstream sensors, right before and after the air-water interface passes the downstream sensor. When the air-water interface is between the two pressure sensors (Figure 10a), the membrane in the upstream sensor undergoes a large deflection as evident from the horizontally elongated particle images, suggesting a high pressure is exerted on the upstream pressure sensor. The downstream sensor on the other hand shows very little membrane deflection as evident from the vertically elongated particle images. Due to the low dynamic viscosity of air and the extremely low flow rate, the contribution of viscous pressure drop of air is largely negligible. Therefor, the pressure difference between the upstream and downstream sensors is essentially due the capillary pressure generated across the interface. However, when the air-water interface passes the downstream sensor (Figure 10b), the upstream sensor immediately resume to its initial condition, with little pressure difference detected between the upstream and downstream sensors, as expected.

Based on the particle images, the capillary pressure across the air-water interface in the microchannel was measured to be 1.54 kPa. A theoretical value of the capillary pressure was calculated using the Young-Laplace equation based on the microchannel dimensions, the water-air surface tension and the receding contact angle[16],

$$p^c = 2\sigma(\frac{1}{w}+\frac{1}{d})\cos\theta \qquad (2)$$

where p^c is the capillary pressure, σ is the surface tension of water (0.072 N/m), w and d are the width (0.096 mm) and depth (0.12 mm) of the microchannel, respectively, and θ (57°) is the receding contact angle of the water phase. Note due to the trapezoidal shape of the cross section, w here was taken at the narrowest point, which is believed to dominate the capillary pressure[16].

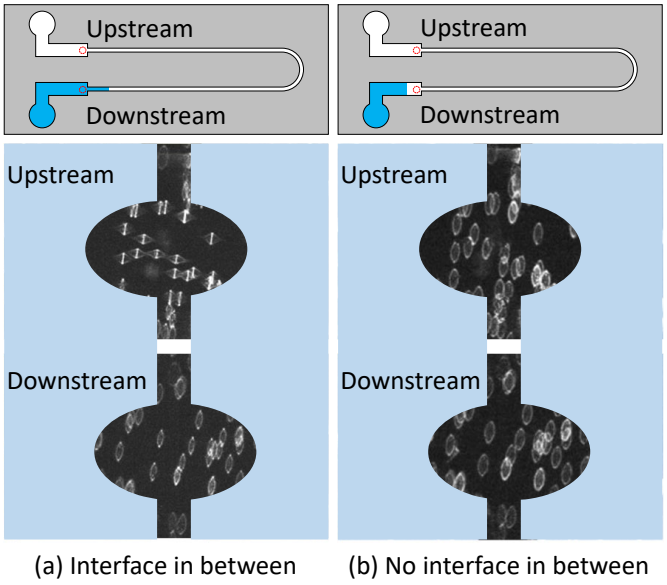

Fig. 10 Particle image shapes of the upstream and downstream sensors before (a) and after (b) the air-water interface passes the downstream sensor. When capillary pressure jump exists between the two sensors (a), the upstream sensor is subject to high pressure; when the interface exits the test channel (b), both sensors are subject to low pressure.

Based on Equation 2 and the physcial values, the theoretical capillary pressure was calculated to be 1.47 kPa, which deviates from the measured value by 0.07 kPa (4.5%), within the measurement uncertainty of 0.07 kPa of the pressure sensor. This result represents a big improvement compared with previous capillary pressure measurement based on interfacial curvature [16].

The last thing to note is that properties of PDMS are known to change over time (*e.g.*, bulk materials get stiffer over time) [46]. To ensure that our results are not significantly impacted by this effect, all the experiments were performed within 10 hours of the calibration. Additionally, a stability test was carried out to determine the change of the calibration curve of the same sensor over 24 hours. The membrane indeed got slightly more rigid over time, leading to a higher pressure in the second test for the same amount of membrane deflection. Although results are not shown, the RMSD between the two curves is found to be 0.035 kPa, which is ∼1.2% of the full scale. Nevertheless, this relatively small shift of material properties further justifies our measurement quality.

4 Conclusions

A membrane-based microfluidic pressure sensor has been successfully designed and fabricated using simple soft lithography. By embedding 1 μm fluorescent particles into the thin membrane, and using Astigmatic Particle Tracking scheme, the membrane deflection is detected based on the shape of the particles. The simple optical readout method and image processing algorithm have led to fast and precise pressure measurements under single and multi-phase flow conditions in the microchannel. The current sensor has a measurement range of 0–2.9 kPa with an accuracy of 70 Pa. The sensor has been successfully applied to measure the pressure drop within a microchannel for single-phase flow of air and DI water. Good agreement has been achieved between the pressure sensor, a commercial pressure transducer and numerical simulation results. Additionally, to the best of our knowledge, the sensor has for the first time successfully measured the capillary pressure across the air-water interface with a 7% deviation from the theoretical value. The capability demonstrated by the pressure sensor is promising and this work opens the door to a renewed understanding of pore-scale physics of multi-phase flow in porous media.

Although the current study only demonstrated the use of two pressure sensors in a microchannel, as the next step a 2D array of pressure taps will be fabricated to enable a true 2D pressure field mapping, which can be achieved by a simple change of the photomask design. Moreover, although not explored in the current study, the sensitivity and measurement range of the pressure sensor can be finely tuned by adjusting parameters such as the pressure sensor size, PDMS membrane thickness, and even the Young's modulus of the PDMS material. A parametric study of the system will be carried out in a future study to gain a better understanding of the device performance, and help to accommodate more challenging measurements, such as 2D pressure mapping of multi-phase flow in porous media. Finally, surface wettability is a well-known issue of the PDMS material. Although the naturally hydrophobic PDMS surfaces can be made hydrophilic by exposing them to an air or oxygen plasma, such modification is known to be unstable [47]. Additionally, PDMS itself is incompatible with many solvents and oils, all of which may limit its application in many multi-phase flow scenarios [48]. To partially alleviate this issue, we will explore different elastic materials and/or different types of coatings to further expand its compatibility.

Author Contributions

Nishagar Raventhiran: Methodology, Data acquisition, Data curation, Writing - Original draft preparation. Razin Sazzad Molla: Methodology, Data acquisition. Kshithij Nandishwara: Software, Data curation, Validation. Erick Johnson: Supervision, Software, Writing- Reviewing and Editing. Yaofa Li: Conceptualization, Methodology, Data acquisition, Data curation, Writing- Reviewing and Editing.

Conflicts of interest

There are no conflicts to declare.

Acknowledgements

This work was performed in part at the Montana Nanotechnology Facility, a member of the National Nanotechnology Coordinated Infrastructure (NNCI), which is supported by the National Science Foundation (Grant ECCS-1542210). This work was partially supported by the Murdock Charitable Trust. We are grateful to the Faculty Excellence Grants and the Norm Asbjornson College of Engineering at Montana State University for their support. We also thank Dr. Andrew Lingley and Dr. Joshua Heinemann at Montana Microfabrication Facility for their help with the device fabrication.

References

1 T. Matsunaga, M. Hosokawa, A. Arakaki, T. Taguchi, T. Mori, T. Tanaka and H. Takeyama, *Analytical chemistry*, 2008, **80**, 5139–5145.

2 M. M. Crane, K. Chung, J. Stirman and H. Lu, *Lab on a Chip*, 2010, **10**, 1509–1517.

3 J. G. Shackman, G. M. Dahlgren, J. L. Peters and R. T. Kennedy, *Lab on a Chip*, 2005, **5**, 56–63.

4 P. J. Lee, T. A. Gaige and P. J. Hung, *Lab on a Chip*, 2009, **9**, 164–166.

5 J. E. McClure, S. Berg and R. T. Armstrong, *Physics of Fluids*, 2021, **33**, 083323.

6 C. Garing, J. A. de Chalendar, M. Voltolini, J. B. Ajo-Franklin and S. M. Benson, *Advances in Water Resources*, 2017, **104**, 223–241.

7 A. L. Herring, J. Middleton, R. Walsh, A. Kingston and A. Sheppard, *Advances in Water Resources*, 2017, **107**, 460–469.

8 R. T. Armstrong, J. E. McClure, M. A. Berrill, M. Rücker, S. Schlüter and S. Berg, *Physical Review E*, 2016, **94**, 043113.

9 W. G. Gray, K. Bruning and C. T. Miller, *Journal of Hydraulic Research*, 2019, **57**, 747–759.

10 H. E. Huppert and J. A. Neufeld, *Annu. Rev. Fluid Mech*, 2014, **46**, 255–272.

11 Y. Li, G. Blois, F. Kazemifar and K. T. Christensen, *Water Resources Research*, 2019, **55**, 3758–3779.

12 Y. Chen, Y. Li, A. J. Valocchi and K. T. Christensen, *Journal of Contaminant Hydrology*, 2018, **212**, 14–27.

13 A. Fakhari, Y. Li, D. Bolster and K. T. Christensen, *Advances in Water Resources*, 2018, **114**, 119–134.

14 Y. Li, F. Kazemifar, G. Blois and K. T. Christensen, *Water Resources Research*, 2017, **53**, 6178–6196.

15 Y. Li, G. Blois, F. Kazemifar and K. T. Christensen, *Measurement Science and Technology*, 2021.

16 N. Karadimitriou, S. Hassanizadeh, V. Joekar-Niasar and P. Kleingeld, *Water Resources Research*, 2014, **50**, 8125–8140.

17 A. Orth, E. Schonbrun and K. B. Crozier, *Lab on a Chip*, 2011, **11**, 3810–3815.

18 I. Zarikos, S. Hassanizadeh, L. van Oosterhout and W. van Oordt, *Transport in porous media*, 2018, **122**, 221–234.

19 Y. Li, R. Grigoriev and M. Yoda, *Physics of Fluids*, 2014, **26**, 122112.

20 Y. Li and M. Yoda, *Experiments in Fluids*, 2014, **55**, 1–11.

21 Y. Li and M. Yoda, *International Journal of Heat and Mass Transfer*, 2016, **102**, 369–380.

22 Y. Zhu, D. S. Antao, K.-H. Chu, S. Chen, T. J. Hendricks, T. Zhang and E. N. Wang, *Journal of Heat Transfer*, 2016, **138**, year.

23 A. Chaudhury, A. Pantazis and N. Chronis, *Sensors and Actuators A: Physical*, 2016, **245**, 63–67.

24 S. H. Aref, H. Latifi, M. I. Zibaii and M. Afshari, *Optics communications*, 2007, **269**, 322–330.

25 M. Abkarian, M. Faivre and H. A. Stone, *Proceedings of the National Academy of Sciences*, 2006, **103**, 538–542.

26 F. Shen, M. Ai, J. Ma, Z. Li and S. Xue, *Micromachines*, 2020, **11**, 914.

27 N. Srivastava and M. A. Burns, *Lab on a Chip*, 2007, **7**, 633–637.

28 C. Hoera, A. Kiontke, M. Pahl and D. Belder, *Sensors and Actuators B: Chemical*, 2018, **255**, 2407–2415.

29 D. Wagner, J. Frankenberger and P. Deimel, *Journal of Micromechanics and Microengineering*, 1994, **4**, 35.

30 W. Song and D. Psaltis, *Optics letters*, 2010, **35**, 3604–3606.

31 K. Chung, H. Lee and H. Lu, *Lab on a Chip*, 2009, **9**, 3345–3353.

32 V. A. ROSSI and M. A. CARPENTER, *Sensors & Transducers*, 2019, **239**, 34–40.

33 T. Jung and S. Yang, *Sensors*, 2015, **15**, 11823–11835.

34 D.-W. Lee and Y.-S. Choi, *Microelectronic Engineering*, 2008, **85**, 1054–1058.

35 X. Liu, Y. Zhu, M. W. Nomani, X. Wen, T.-Y. Hsia and G. Koley, *Journal of Micromechanics and Microengineering*, 2013, **23**, 025022.

36 C.-Y. Wu, W.-H. Liao and Y.-C. Tung, *Lab on a Chip*, 2011, **11**, 1740–1746.

37 C.-L. Dai, P.-W. Lu, C. Chang and C.-Y. Liu, *Sensors*, 2009, **9**, 10158–10170.

38 P.-J. Chen, D. C. Rodger, S. Saati, M. S. Humayun and Y.-C. Tai, *Journal of Microelectromechanical Systems*, 2008, **17**, 1342–1351.

39 X. Zhou, R. Zhang, L. Li, L. Zhang, B. Liu, Z. Deng, L. Wang and L. Gui, *Lab on a Chip*, 2019, **19**, 807–814.

40 C. Cierpka, M. Rossi, R. Segura and C. Kähler, *Measurement Science and Technology*, 2010, **22**, 015401.

41 Y. Ichikawa, K. Yamamoto and M. Motosuke, *Microfluidics and Nanofluidics*, 2018, **22**, 1–9.

42 Y. Xia and G. M. Whitesides, *Angewandte Chemie International Edition*, 1998, **37**, 550–575.

43 J. H. Koschwanez, R. H. Carlson and D. R. Meldrum, *PLoS one*, 2009, **4**, e4572.

44 B. S. Hardy, K. Uechi, J. Zhen and H. P. Kavehpour, *Lab on a Chip*, 2009, **9**, 935–938.

45 M. Bahrami, M. Yovanovich and J. Culham, International Conference on Nanochannels, Microchannels, and Minichannels, 2005, pp. 269–280.

46 M. Kim, B.-U. Moon and C. H. Hidrovo, *Journal of Micromechanics and Microengineering*, 2013, **23**, 095024.

47 N. Karadimitriou, M. Musterd, P. Kleingeld, M. Kreutzer, S. Hassanizadeh and V. Joekar-Niasar, *Water Resources Research*, 2013, **49**, 2056–2067.

48 J. N. Lee, C. Park and G. M. Whitesides, *Analytical chemistry*, 2003, **75**, 6544–6554.